NUCL SCI TECH (2018) 29:147
https://doi.org/10.1007/s41365-018-0479-9

Evaluation of radiation environment in the target area of fragment separator HFRS at HIAF

Yao Yang[1,2] · You-Wu Su[1] · Wu-Yuan Li[1] · Jun-Kui Xu[1] · Chong Xu[1] · Wei-Wei Yan[1] · Wang Mao[1]

Received: 16 August 2017 / Revised: 16 January 2018 / Accepted: 12 March 2018 / Published online: 1 September 2018

Abstract In this work, the radiation environment in the target area of a fragment separator is evaluated using FLUKA code. The energy deposition in quadrupole coils is presented to provide guidance for a radiation-resistant magnets design. Results show that neutrons dominate in the prompt radiation field. A compact shielding design is recommended for high radiation areas along with the minimization of air activation in the tunnel in order to minimize the radiation effect on nearby beam lines. The displacements per atom results for the graphite target and copper coils indicate that the effect is insignificant. In addition, the activation level of the target is estimated for workers under possible hands-on maintenance condition.

Keywords Fragment separator · FLUKA · Radiation levels · Radiation damage

1 Introduction

The application of radioactive ion beams (RIBs) in nuclear physics and astrophysics led to the discovery of many new physical phenomena since it was first employed in Lawrence Berkeley Laboratory (LBL) by Tanihata in 1985 [1]. There are two prevalent approaches to produce RIBs. One is in-flight separation, which is also called the projectile fragmentation (PF) method, and the other is the isotope separation on line (ISOL) method [2–4]. Two radioactive ion beam lines RIBLL1 and RIBLL2 have been constructed in the Heavy Ion Research Facility in Lanzhou (HIRFL) and have been operated since 1998 and 2008, respectively. RIBs produced in both RIBLL1 and RIBLL2 are based on in-flight method and can provide multiple secondary beams in different energy ranges. Many experiments such as interaction cross section measurement, proton halo studies, nuclear astrophysics studies, new isotope identification have been carried out using these two beam lines [5–9]. At present, there are many already existing or under-plan RIBs facilities worldwide. FRS and Super-FRS in GSI, RIPS and Big-RIPS in RIBF, FRIB in MSU, ISAC-I and ISAC-II in TRIUMF, and HIE-ISOLDE in CERN are a few examples of such facilities [3, 4, 7, 10–15]. These facilities function in different energy regions, allowing for different reaction mechanisms, and therefore, they vary in the range of isotopes.

A new radioactive ion beam line named HIAF FRagment Separator (HFRS) will be built at High Intensity heavy ion Accelerator Facility (HIAF) by the Institute of Modern Physics (IMP) in the near future. The in-flight separation method will be employed in HFRS to produce RIBs. A schematic view of the HFRS in HIAF is shown in Fig. 1 [16]. It is located between the booster ring (BRing) and high-precision spectrometer ring (SRing). It consists of a two-stage magnetic system, the pre-separator and the main-separator, both of which are achromatic systems. The pre-separator is used to distinguish the primary beams from the secondary beams. The unreacted primary beams are stopped in the beam dumps located in the pre-separator.

This work was supported by the National Key Research and Development Program of China (No. 2017YFC0107700).

✉ You-Wu Su
suyouwu@impcas.ac.cn

1 Institute of Modern Physics, Chinese Academy of Sciences, Lanzhou 730000, China

2 University of Chinese Academy of Sciences, Beijing 100049, China

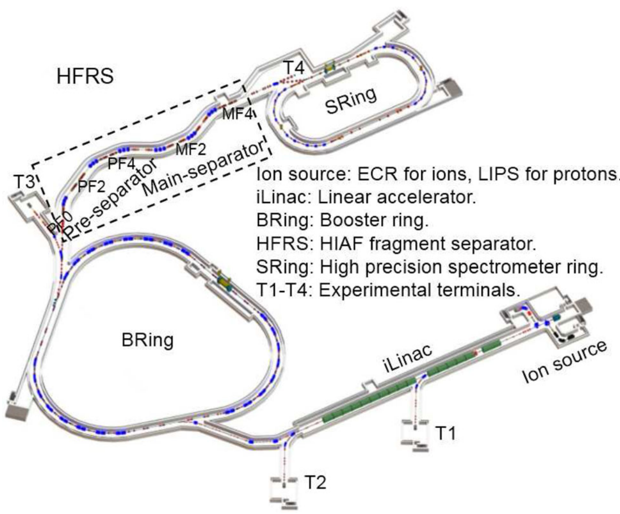

Fig. 1 (Color online) Layout of HFRS in HIAF

The secondary beams are separated and purified in the main-separator and finally transported to the terminals or SRing for conducting scientific research. The design parameters of the HFRS are listed in Table 1 and compared with other in-flight fragment separators [3–11, 17].

The high-energy and high-intensity primary beams are made incident on a target with a thickness of a few g/cm^2, and the production and separation of interesting RIBs can induce a strong and complex radiation field in the HFRS, especially in the target and beam dump areas. High-yield neutrons with strong penetrability dominate the prompt radiation field around high-energy heavy-ion accelerators [18, 19]. The main objective of this study is to analyze and evaluate the prompt radiation field in the target area by using the FLUKA code and provide parameters for further shielding calculation. The magnets behind the target are exposed to a high-level radiation environment; therefore, the energy deposition in magnet coils has been calculated for the radiation-resistant magnets design. Radiation damage evaluations for the target and magnet coils are also presented. In the end, in view of a possible hands-on maintenance of target by workers, the radionuclides produced in the target and the corresponding residual dose rate are estimated.

2 Monte Carlo calculations

The simulations were performed with the FLUKA Monte Carlo code version 2011. 2c.5. Nuclear interactions induced by ions were treated by linking different physical models such as DPMJET, RQMD, and BME [20, 21]. The transport of low-energy neutrons ($E < 20$ MeV) was performed using its own neutron cross section library, wherein the energy of interest was divided into a given number of intervals [20].

A rotated target with different thicknesses was employed in the HFRS. This design was similar to the Super-FRS at GSI [22], target-E at PSI [23], and Big-RIPS at RIKEN [24]. In this study, a static and circular disk of target with inner radius $R_1 = 13.5$ cm and outer radius $R_2 = 22.5$ cm was adopted in the model. The primary beams were considered incident on a point at $R = (R_1 + R_2)/2 = 18.0$ cm. The beam spot on target was assumed to be $\pm$ 1 and $\pm$ 2 mm in the horizontal and vertical directions, respectively. The geometry model built in FLUKA is shown in Fig. 2. The target and a 40-cm-long cube iron shielding block were installed in the vacuum chamber. Three quadrupole magnets Q1, Q2, and Q3 were placed 130 cm, 330 cm, and 508 cm away from the target site, respectively.

The magnetic field in quadrupoles was activated by the MGNFIELD and ASSIGNMA cards by compiling the user routine magfld.f with FORTRAN programming. Secondary particle yields were scored through the USRBDX card at 0°, 15°, 30°, 60°, and 90° angles; the range of each angle was $\pm$ 2.5° except at 0°. For forward angle measurements, the statistical error was higher compared with that for other

Table 1 Design parameters of HFRS compared with those of other in-flight facilities

Facility	Location	Ω (msr)	$\Delta p/p$	$B\rho_{max}$ (Tm)	Momentum resolution	Length (m)
HFRS	IMP (China)	1.4	± 2.0	15.0	1500	152.0
RIBLL1	IMP (China)	> 7.0	± 5.0	4.2	1200	35.0
RIBLL2	IMP (China)	2.0	± 1.0	10.64	1200	55.0
LISE	GANIL (France)	1.0	± 2.5	3.2	800	18.0
FRS	GSI (Germany)	0.2	± 1.0	18.0	1500	73.0
Super-FRS	GSI (Germany)	0.8	± 2.5	20.0	1500	140.0
RIPS	RIBF (Japan)	5.0	± 3.0	5.76	1500	21.0
Big-RIPS	RIBF (Japan)	8.0	± 3.0	9.0	1290/3300	77.0
COMBAS	Dubna (Russia)	6.0	± 10.0	4.5	4360	14.5
A1200	NSCL (USA)	0.8–4.3	± 1.5	5.4	700–1500	22.0
A1900	NSCL (USA)	8.0	± 2.25	6.0	2900	35.0

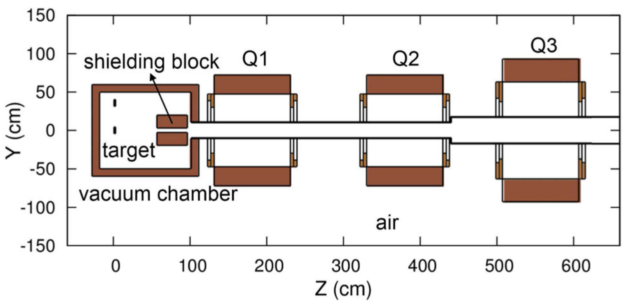

Fig. 2 (Color online) FLUKA model for target area of HFRS

angles; hence, the angular range was set to ± 4.0° in the 0° direction. Physical process for precision nuclear interaction was set by the PHYSICS card to activate electromagnetic dissociation, heavy fragment evaporation, and coalescence. The dose equivalent was calculated with the help of the USRBIN card together with the AUXSCORE card by linking the fluence-to-dose conversion coefficients. The IRRPROFI card and DCYTIMES card were used to define the irradiation time and decay time, respectively. The residual radionuclides were scored by the RESNUCLE card after the bombardment ended. Moreover, the value of the radiation damage threshold E_{th} was obtained using the NJOY99 code [25] and set through the MAT-PROP card. The DEFAULTS card used in simulation was with the PRECISIO option. Cartesian binning, R–Φ–Z binning, and regional scoring methods were used in the calculation.

3 Results and discussion

Neutron yields depend on the projectile type, incident energy, and target material. Typical beam–target combinations of HFRS together with the FLUKA-calculated neutron yields are listed in Table 2. The statistical error of yields is less than 2%. The results indicate that the highest neutron yield is achieved at 800 MeV/u ^{238}U impinging on a 4.0 g/cm^2 graphite target. Hence, the following calculations are based on this situation and the beam intensity is 3.33×10^{10} pps (particles per second).

3.1 Energy deposition

The quadrupole magnets in the target area and the dipole magnets in the beam dump area are exposed to a high-level radiation environment. Hence, radiation-resistant magnets need to be employed. In this work, the energy deposition in quadrupole coils is studied and presented. Table 3 lists the radiation limit of various magnet materials [26].

In calculation, coils were assumed to be made of pure copper, and for each quadrupole, the coils were divided into five parts for dose calculation: the first and second layers in the front edge, third part in the iron yoke, and the fourth and fifth layers in the back edge, as shown in Fig. 4a. The third part coil in a simplified geometry model of Q1 is shown in Fig. 3. Q2 is the same as Q1, while Q3 has the same structure but with different parameters.

The lifetime of the magnets is determined by the peak dose in the coil. In this work, the energy deposition is scored with R–Φ–Z binning method, and very small binnings are used to determine the peak dose. R is given by the inner and outer radii of each coil and is divided into 120 bins. Φ is the azimuthal angle around Z (beam) axis and is set to 180 bins. Z-bins value is set to 400. The comparison of peak dose in different parts of coils is scaled to the same mesh size with 0.15 cm, 2°, and 0.25 cm as the values for R, Φ, and Z, respectively. To convert energy deposition expressed in GeV/cm^3/pri to Gy/s (J/kg/s), the results were multiplied by $1.0 \times 10^{12} \times C_{e^-} \times I/\rho$, where C_{e^-} is the electron charge, I is the beam intensity (pps), and ρ is the density of the material (g/cm^3).

In view of the possible contribution of charged particles to the energy deposition on the coils, the magnetic field in the quadrupoles was added as discussed above. Peak dose distribution in three quadrupole coils is shown in Fig. 4a. The results indicate that peak dose in the coil decreased gradually along the beam direction. Moreover, the peak dose in each part of Q1 was found to be greater than that in the corresponding part in Q2 and Q3. Peak dose in the first layer in the front edge of Q1 was 0.026 Gy/s, which is

Table 2 Neutron yields for different beam–target combinations

Ion	Energy (MeV/u)	Target	Yields (n/pri)
^{86}Kr	500	Be (1.0 g/cm^2)	2.8
^{86}Kr	1500	C (4.0 g/cm^2)	10.8
^{12}C	900	Be (8.0 g/cm^2)	3.5
^{124}Xe	1000	C (4.0 g/cm^2)	14.1
^{238}U	800	C (2.5 g/cm^2)	18.9
^{238}U	800	C (4.0 g/cm^2)	28.9

Table 3 Radiation limit of various magnet materials

Material	Radiation limit (Gy)
NbTi	$\approx 5 \times 10^8$
Nb_3Sn	$\approx 5 \times 10^8$
Copper	$> 10^{10}$
Ceramics (Al_2O_3, MgO, etc.)	$> 10^9$
Organics	10^6–10^8

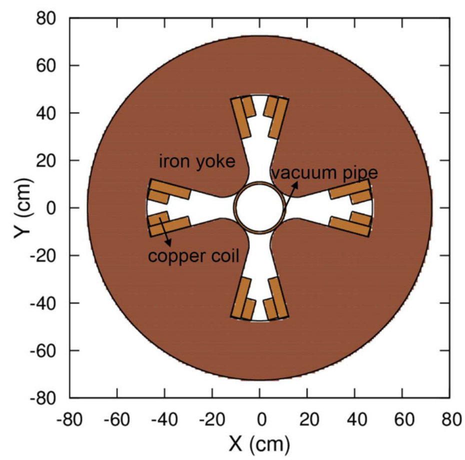

Fig. 3 (Color online) The third part coil in a simplified geometry model of Q1

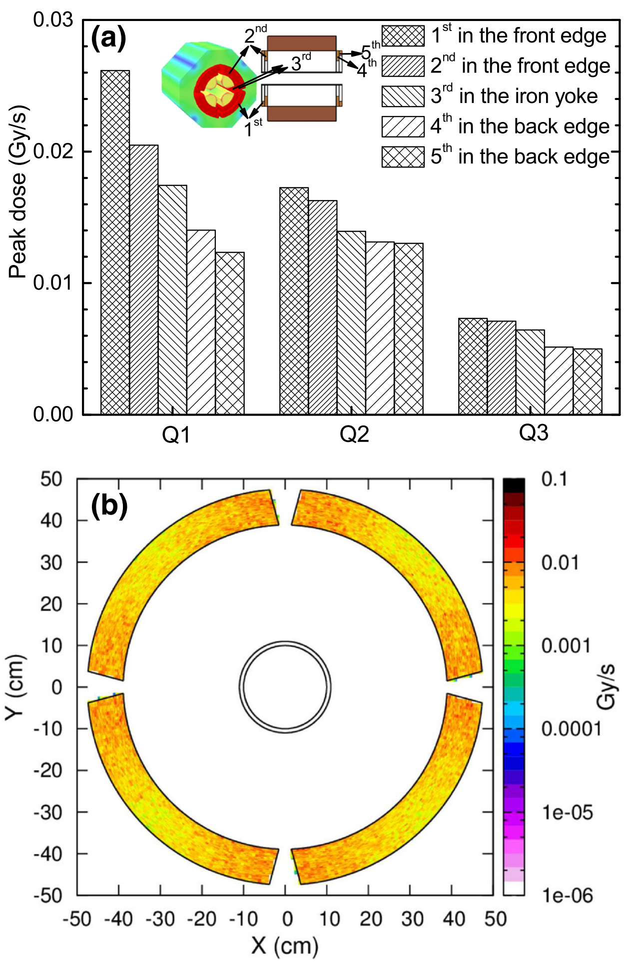

Fig. 4 (Color online) Dose distribution in three quadrupole coils (**a**) and in the first layer in the front edge of Q1 (**b**)

about a factor of 1.6 and 3.6 higher compared to that in Q2 and Q3. Figure 4b shows the dose distribution in the first layer in the front edge of Q1. Further, the results showed that neutrons are the major contributors to the energy deposition. In our simulation, a hollow iron shielding block was installed in the vacuum chamber to prevent the secondary particles. This can dramatically reduce the energy deposition in the coils, especially in Q1. Similar protection designs have been reported for other facilities [27–29].

For other coil materials such as Nb_3Sn and NbTi listed in Table 3, owing to the almost similar density as copper, similar results as in the case of copper were obtained. Assuming that the operation time of HFRS is 4000 h per year, the accumulated dose in the first layer in the front edge of Q1 will be 4.176×5 Gy per year. In this case, copper can meet the operational requirement based on the radiation limit listed in Table 3. However, the dose limit of organic insulators like epoxy resin ranges from 10^6 to 10^8 Gy, which is more radiation sensitive than other materials. Therefore, the energy deposition on organic insulators needs careful consideration. The results are obtained by replacing the copper coil with epoxy resin. As the insulator is very thin, the binning size is very small compared to the size used in copper. The results indicate that the peak dose in epoxy resin is 0.062 Gy/s, which is twice that of copper. Hence, metal oxide insulation materials such as MgO and Al_2O_3 are suggested for the magnet design. A typical radiation-resistant cable is mineral-insulated cable (MIC), for which the ceramic insulators are used. The cable allows direct water cooling with a hole in the center of the conductor; therefore, high current density can be achieved.

3.2 Prompt radiation field analysis

Neutron energy spectrum is shown in Fig. 5a. Broad peaks appear in the forward angles (0° and 15°) and are mainly caused by the high-energy neutrons shown in the results. These neutrons are emitted via the intra-nuclear cascade process with the same energy and direction as the incident particles. As the neutron energy increases, the distribution is more forward peaked as shown in Fig. 5a and b. In backward angles (larger angles), the proportion of high-energy neutrons is reduced and the peaks disappear gradually. Meanwhile, low-energy neutrons dominate in the backward angles, where the neutrons are mainly produced from the evaporation process of the compound nucleus and emit isotropically. With the increase in angle, the photon yields first decrease slightly, reaching a minimum at 90°, then increase gradually and remains unchanged at angles greater than 120°, as shown in Fig. 5b.

Figure 6a, b shows the prompt radiation field of the neutron and the photon, respectively. The results indicate that the neutron dose rate is about two orders of magnitude higher than the photon. For example, in the lateral direction

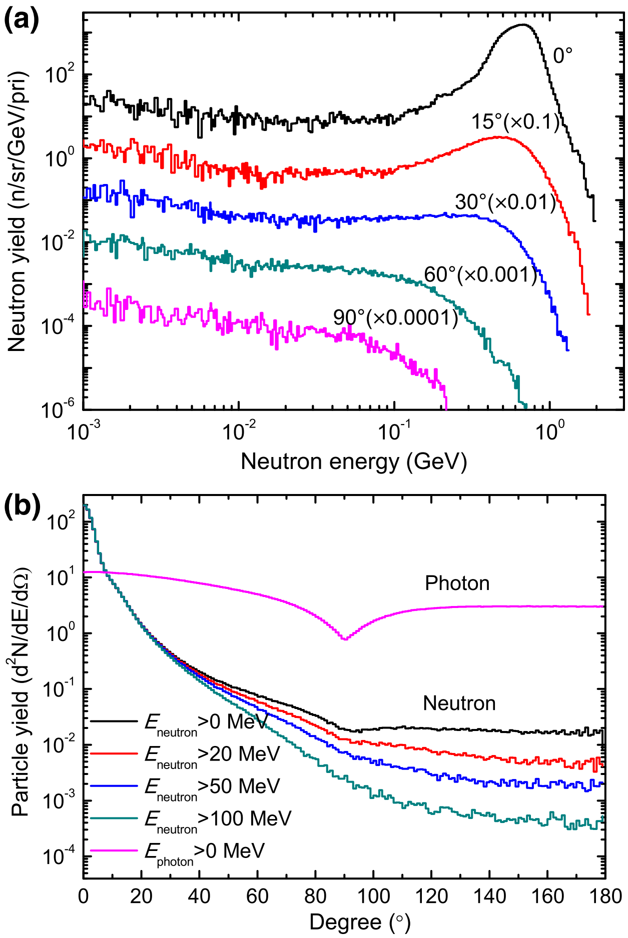

Fig. 5 (Color online) Neutron energy spectrum (**a**) and angular distribution of neutron and photon yield (**b**)

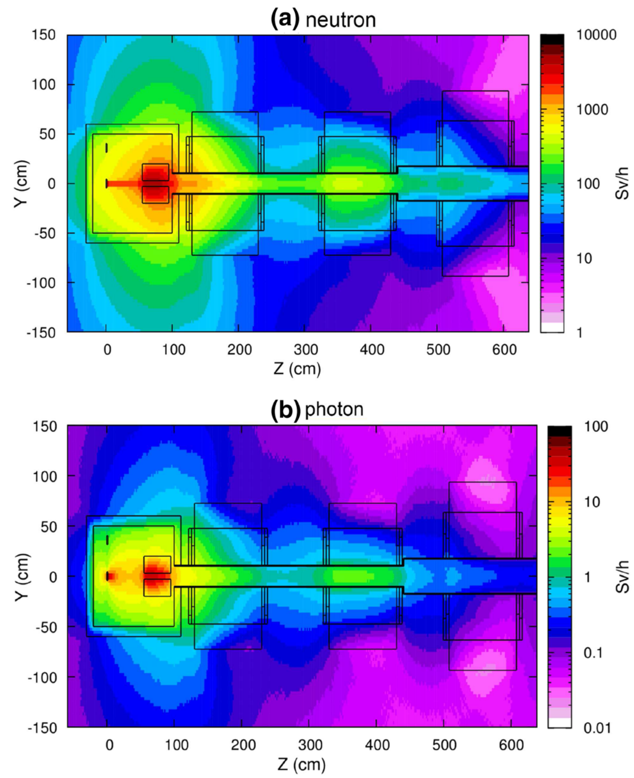

Fig. 6 (Color online) Neutron (**a**) and photon (**b**) dose equivalent in target area

of vacuum chamber, the neutron and photon dose rates are 2.20×10^5 mSv/h and 6.29×10^2 mSv/h, and 1.67×10^5 mSv/h and 5.71×10^2 mSv/h in the lateral direction of Q1, respectively. Along the beam direction, the dose rate gets reduced due to the shielding of quadrupoles. In Q2 and Q3 lateral directions, the dose rate is 1.54×10^4 and 5.32×10^3 mSv/h for neutron and 62.7 and 39.0 mSv/h for photon, respectively. Subsequent shielding calculations were based on these results. In order to reduce the radiation effect on nearby beam lines, air activation in the tunnel was minimized and a compact shielding design was employed in the pre-separator of HFRS from the target area to focal plane PF2 (shown in Fig. 1).

3.3 Radiation damage

Displacements per atom (DPA) is a measure of the amount of primary radiation damages in irradiated materials. The results of DPA and corresponding non-ionizing energy losses due to energy deposition (shown as NIEL-DEP in FLUKA) caused by different particles are presented in Fig. 7. The results show that the uranium beam-induced DPA decreased slightly with the increase in depth, whereas, for neutron, proton, and photon, the condition was found to be different; it increased first and then nearly stabilized at a certain value. For the uranium beam, the magnitude of the displacement rate is in 10^{-7} dpa/s, followed by about 10^{-10} dpa/s for neutron and proton, while it is least at about 10^{-16} dpa/s for photon. Hence, for the graphite target, primary uranium beam-induced radiation damages are the main contributions. The total DPA is 2.20

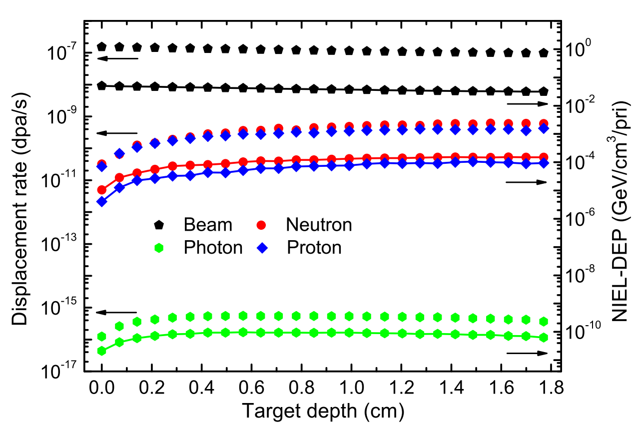

Fig. 7 (Color online) Depth profile of damage induced in target by different particles

for 4000 h of operation per year. As graphite is used as absorber in the beam dumps, the damages will be more severe due to the fact that all unreacted primary beams will be stopped in the graphite. For copper coils, the largest radiation damage appears in the first layer in the front edge of Q1. Neutrons are the main contributors, and the damages induced by other particles are almost negligible; the total DPA is 1.53×10^{-3} per year. Hence, the DPA results are expected to be insignificant for the graphite target and copper coil.

In addition to the displacement damages, helium and hydrogen gas atoms participate in transmutation reactions during irradiation process. This also has a negative effect on mechanical properties. Hydrogen is believed to diffuse out of graphite due to the high temperature produced during irradiation, while helium can accumulate in bubbles, which can grow at grain boundaries. These factors will lead to embrittlement and swelling in irradiated graphite and can shorten the lifetime. Other factors such as radiation heating and mechanical stress will be discussed in the following work using the ANSYS software.

3.4 Residual activity in target

Activation calculations are given under 30 days of irradiation. At the end of bombardment, 20 more radionuclides are produced in graphite target. The dominant radionuclides are depicted in Fig. 8. Short-lived isotopes like ^{13}B, ^{12}Be, ^{12}N, ^{9}C, ^{9}B, and ^{9}Li will rapidly decay to a very low level. After one-hour decay, the main contributions are ^{11}C, ^{7}Be, and ^{3}H, while later, up to six hours, ^{7}Be and ^{3}H become dominant. Most of the tritium will evaporate during irradiation as discussed above, so in a long operation period the activated graphite for target and beam dumps in HFRS might be a source of ^{7}Be and ^{10}Be. In order to move the activated components, radiation shielding bottle at PSI has been designed to move activated parts like target and beam dumps to a storage cell [23].

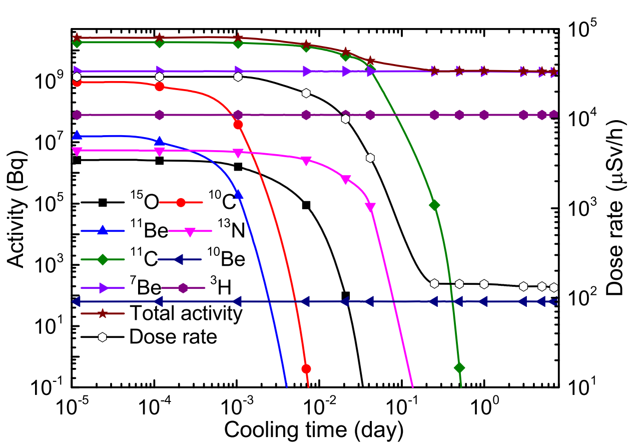

Fig. 8 (Color online) Dominant radionuclides and residual dose rate at 20 cm from target surface

Residual dose rate at 20 cm from the surface of the target after different cooling times has also been evaluated for possible hands-on maintenance condition. The results are shown on the right *Y*-axis of Fig. 8. After 1-h cooling, the dose rate is 3.64×10^3 μSv/h, while later, up to 6 h or longer, the dose rate decreased by two orders of magnitude and appeared to be unchanged at about 1.44×10^2 μSv/h. For conservative calculation, the target will be changed after 6 h of turning down the accelerator, each time takes one hour, and it is done 6 times in a year, so the annual dose is about 0.86 mSv for the workers. This value is below the dose limit 20 mSv/a for occupational radiation workers. In case of short-time cooling, it is not advisable to conduct hands-on maintenance. Hence, remote handling needs to be executed.

4 Summary

Primary radiation environment evaluations have been conducted for the target area of fragment separator HFRS in HIAF by using the FLUKA program. The energy deposition in the quadrupole coils was analyzed. The largest value appeared in the first layer in the front edge of Q1, and the total dose was 4.176×10^5 Gy for 4000 h of operation in a year. In this case, copper coil can meet the operational requirement. However, for insulators like epoxy resin, the condition was opposite. Therefore, cables with ceramic insulators like MIC were recommended. The prompt radiation field has also been investigated, and the results indicate that neutrons were the main contributors. Compact shielding design was advised for the high-radiation areas in the pre-separator. The results of radiation damages on graphite target and copper coils show that the effect was almost negligible. Activation calculations show that long-lived radionuclides in the graphite target were the source of residual dose rate. The annual dose for radiation workers was below the dose limit of occupational exposure, while in the case of short-time cooling, remote handling needs to be executed.

References

1. I. Tanihata, H. Hamagaki, O. Hashimoto, Measurements of interaction cross sections and nuclear radii in the light p-shell region. Phys. Rev. Lett. **55**, 2676 (1985). https://doi.org/10.1103/PhysRevLett.55.2676
2. B. Harss, P. R. C., K.E. Rehm, Production of radioactive ion beams using the in-flight technique. Rev. Sci. Instrum. **71**, 380–387 (2000). https://doi.org/10.1063/1.1150211

3. S. Agosteo, G. Fehrenbacher, M. Silari, Attenuation curves in concrete of neutrons from 1 GeV/u C and U ions on a Fe target for the shielding design of RIB in-flight facilities. Nucl. Instrum. Methods B. **226**, 231–242 (2004). https://doi.org/10.1016/j.nimb.2004.06.038
4. Y. Blumenfeld, T. Nilsson, P. Van Duppen, Facilities and methods for radioactive ion beam production. Phys. Scr. **T152**, 014023 (2013). https://doi.org/10.1088/0031-8949/2013/T152/014023
5. Z.Y. Sun, W.L. Zhan, Z.Y. Guo, RIBLL, the radioactive ion beam line in Lanzhou. Nucl. Instrum. Methods A. **503**, 496–503 (2003). https://doi.org/10.1016/S0168-9002(03)01005-2
6. J.J. He, S.W. Xu, P. Ma, A new low-energy radioactive beam line for nuclear astrophysics studies in China. Nucl. Instrum. Methods A. **680**, 43–47 (2012). https://doi.org/10.1016/j.nima.2012.03.040
7. Y.L. Ye, Development of RIB facilities in Asia. Nucl. Instrum. Methods B. **317**, 201–203 (2013). https://doi.org/10.1016/j.nimb.2013.07.053
8. Z.Y. Sun, W.L. Zhan, Z.Y. Guo, Separation and identification of isotopes produced from ^{20}Ne + Be reaction by radioactive ion beam line in Lanzhou. Chin. Phys. Lett. **15**, 790–792 (1998). https://doi.org/10.1088/0256-307X/15/11/004
9. J.W. Xia, W.L. Zhan, B.W. Wei, The heavy ion cooler-storage-ring project (HIRFL-CSR) at Lanzhou. Nucl. Instrum. Methods A. **488**, 11–25 (2002). https://doi.org/10.1016/S0168-9002(02)00475-8
10. G. Münzenberg, Radioactive beams at GSI. Prog. Part. Nucl. Phys **46**, 335–342 (2001). https://doi.org/10.1016/S0146-6410(01)00140-5
11. T. Kubo, M. Ishihara, N. Inabe, The RIKEN radioactive beam facility. Nucl. Instrum. Methods B. **70**, 309–319 (1992). https://doi.org/10.1016/0168-583X(92)95947-P
12. S. Gales, SPIRAL2 at GANIL: next generation of ISOL facility for intense secondary radioactive ion beams. Nucl. Phys. A. **834**, 717c–723c (2010). https://doi.org/10.1016/j.nuclphysa.2010.01.130
13. P. Bricault, ISAC-I and ISAC-II: present status and future perspectives. Eur. Phys. J. Spec. Top **150**, 227–232 (2007). https://doi.org/10.1140/epjst/e2007-00310-9
14. Y. Romanets, A.P. Bernardes, A. Dorsival, Radiation protection, radiation safety and radiation shielding assessment of HIE-ISOLDE. Radiat. Prot. Dosim. **155**, 351–363 (2013). https://doi.org/10.1093/rpd/nct005
15. M. Grieser, Y.A. Litvinov, R. Raabe et al., Storage ring at HIE-ISOLDE. Eur. Phys. J. Spec. Top **207**, 1–117 (2012). https://doi.org/10.1140/epjst/e2012-01599-9
16. X. Chen, L.N. Sheng, J.C. Yang, Separation performance research of superconducting fragment separator. High. Power. Laser. Part. Beams. **29**, 128–135 (2017). https://doi.org/10.11884/HPLPB201729.160552. **(in Chinese)**
17. D.J. Morrissey, B.M. Sherrill, Radioactive nuclear beam facilities based on projectile fragmentation. Philos. Trans. R. Soc. B. **356**, 1985–2006 (1998). https://doi.org/10.1098/rsta.1998.0260
18. P.K. Sarkar, Neutron dosimetry in the particle accelerator environment. Radiat. Meas. **45**, 1476–1483 (2010). https://doi.org/10.1016/j.radmeas.2010.07.001
19. C.B. Fulmer, H.M. Butler, W.F. Ohnesorge et al., Fast neutron dose equivalent rates in heavy ion target areas. IEEE Trans. Nucl. Sci **26**, 2216–2218 (1979). https://doi.org/10.1109/TNS.1979.4329842
20. G. Battistoni, F. Cerutti, A. Fassò, The FLUKA code: description and benchmarking. AIP Conf. Proc. **896**, 31–49 (2007). https://doi.org/10.1063/1.2720455
21. F. Ballarini, G. Battistoni, M. Brugger et al., The physics of the FLUKA code: recent developments. Adv. Space Res. **40**, 1339–1349 (2007). https://doi.org/10.1016/j.asr.2007.05.0315
22. N.A. Tahir, H. Weick, H. Iwase, Calculations of high-power production target and beamdump for the GSI future Super-FRS for a fast extraction scheme at the FAIR Facility. J. Phys D. Appl. Phys. **38**, 1828 (2005). https://doi.org/10.1088/0022-3727/38/11/023
23. G. Heidenreich, Carbon and beryllium targets at PSI. AIP Conf. Proc. **642**, 122–124 (2002). https://doi.org/10.1063/1.1522602
24. A. Yoshida, K. Morita, K. Morimoto, High-power rotating wheel targets at RIKEN. Nucl. Instrum. Methods A. **521**, 65–71 (2004). https://doi.org/10.1016/j.nima.2003.11.408
25. R.E. Macfarlane, A.C. Kahler, Methods for processing ENDF/B-VII with NJOY. Nucl. Data. Sheets **111**, 2739–2890 (2010). https://doi.org/10.1016/j.nds.2010.11.001
26. M.E. Sawan, P.L. Walstrom, Superconducting magnet radiation effects in fusion reactors. Fus. Sci. Technol. **10**, 741–746 (1986). https://doi.org/10.13182/FST86-A24829
27. M. Winkler, M. Svedentsov, K.H. Behr, Radiation resistant quadrupole magnet for the Super-FRS at FAIR. IEEE Trans. Appl. Supercond. **16**, 415–418 (2006). https://doi.org/10.1109/TASC.2005.864253
28. A.F. Zeller, V. Blideanu, R.M. Ronningen et al., Radiation resistant magnets for the RIA fragment separator. in *Proceedings of IPAC05, Knoxville, USA*, 2005. https://doi.org/10.1109/PAC.2005.1591056
29. R. Ronningen, G. Bollen, V. Blideanu et al., Radiation simulations and development of concepts for high power beam dumps, catchers and pre-separator area layouts for the fragment separators for RIA. in *Proceedings of IPAC05, Knoxville, USA*, 2005. https://doi.org/10.1109/PAC.2005.1591550